Energy Conversion and Management 357 (2026) 121431

Contents lists available at ScienceDirect

Energy Conversion and Management

journal homepage: www.elsevier.com/locate/enconman

# Hydrogen's role in mitigating emissions variability: A chemical kinetic-thermodynamic digital framework for cleaner combustion technologies

P. Gabana [a,*], A. Cova-Bonillo [b], J.M. Herreros [b], A. Tsolakis [b]

[a] Department of Energy and Fluid Mechanics Engineering, University of Valladolid, Paseo del Cauce 59, E-47011 Valladolid, Spain
[b] Department of Mechanical Engineering, School of Engineering, University of Birmingham, Birmingham B15 2TT, UK

ARTICLE INFO

*Keywords:*
Spark-ignition engine
Hydrogen-gasoline mixture
Emissions
Chemical kinetics
Two-zone thermodynamic model
Cycle-to-cycle variations

ABSTRACT

The combustion process in spark-ignition (SI) engines inherently presents cycle-to-cycle variations (CCV), leading to engine instability and variability in emissions formation. This work develops a digital framework that integrates chemical kinetics and a two-zone thermodynamic diagnostic model to understand the role of hydrogen in mitigating CCV and its impact on emissions formation. The framework predicts the crank angle degree resolved evolution of CCV of CO, $H_2$, NO, and $N_2O$ in the engine combustion chamber's burned gas zone. The framework is calibrated with experimental results from an SI engine working with gasoline-hydrogen fuel mixtures under stoichiometric and lean combustion conditions.

This investigation has revealed that the formation of nitrogen-based emissions, particularly NO, exhibits higher variability than CO and exhaust unburnt $H_2$, with coefficients of variation ranging from 7% to 35%. The high NO variability is attributed to the rapid decrease in NO destruction rates (i.e., kinetic "freezing") at different in-cylinder pressure and temperature conditions within each thermodynamic cycle. It is elucidated that $N_2O$ formation occurs predominantly during the expansion and exhaust strokes. New knowledge has been created to understand how the thermochemical properties of hydrogen reduce NO cycle-to-cycle variability. A synergistic effect is unveiled, hydrogen enrichment leads to an engine operational shift towards a more dilute state (i.e., increased residual gases), where hydrogen's combustion-enhancing properties (e.g., high flame speed, low ignition energy) are crucial for stabilising combustion and thus reducing NO formation variability. Furthermore, the work proposes a new predictive statistical model capable of describing NO dispersion using only the residual–gas fraction and the mean NO level, offering a practical tool for engine calibration and emissions control. Research findings can guide the development of emissions abatement technologies for combustion-based powertrains operating with hydrogen under lean combustion conditions, where conventional catalysts are less effective and understanding gains are highly significant. The proposed digital framework offers an emissions variability predictive tool facilitating the stable operation of clean powertrain for future energy systems.

## 1. Introduction

The transportation sector, responsible for approximately 25% of total EU $CO_2$ emissions in 2022 [1], necessitates a transition towards sustainable energy pathways. In this context, alternative fuels, particularly hydrogen, have gained prominence due to their potential for substantial $CO_2$ emission reductions [2,3]. The transition towards hydrogen is further reinforced by strong institutional and industrial support in Europe [4] and worldwide [5].

Hydrogen has a carbon-free molecular structure, being a strong candidate for use in internal combustion engines (ICEs) aimed to reduce transport-related $CO_2$ emissions [6,7]. The fast laminar combustion speed of hydrogen and its wide flammability limits can improve combustion efficiency. However, the sustainable development of transportation using hydrogen energy systems faces technical issues. These challenges include efficient and safe storage due to its low density, the need for a developed infrastructure for transportation and dispensing, and significant abnormal combustion issues such as knock, backfire, and pre-ignition [8–11]. In this context, hydrogen enrichment is being utilized to enhance the slow oxidation kinetics of carbon-free ammonia blends [12,13], where the high laminar flame speed of $H_2$ is essential for

* Corresponding author.
*E-mail addresses:* pedro.gabana@uva.es (P. Gabana), j.herreros@bham.ac.uk (J.M. Herreros).

https://doi.org/10.1016/j.enconman.2026.121431
Received 22 October 2025; Received in revised form 2 March 2026; Accepted 29 March 2026
Available online 3 April 2026

**Nomenclature**

| | |
|---|---|
| AFR | Air-Fuel Ratio |
| ATDC | After Top Dead Center |
| CA | Crank Angle |
| CAD | Crank Angle Degree |
| CCV | Cycle-to-Cycle Variations |
| CDF | Cumulative Distribution Function |
| CoV | Coefficient of Variation |
| EI-MS | Electron Impact Ionization Mass Spectrometry |
| EU | European Union |
| EVO | Exhaust Valve Opening |
| FTIR | Fourier Transform Infrared |
| G | Gasoline |
| GDI | Gasoline Direct Injection |
| HRR | Heat Release Rate |
| ICEs | Internal Combustion Engines |
| IMEP | Indicated Mean Effective Pressure |
| IVC | Intake Valve Closing |
| *LHV* | Lower Heating Value |
| M | Mixture (Gasoline-Hydrogen) |
| MFB | Mass Fraction Burned |
| PDF | Probability Density Function |
| $P_{exp}$ | Experimental Instantaneous Pressure |
| PRF | Primary Reference Fuel |
| ROP | Rate of Production |
| SI | Spark Ignition |
| $T_b$ | Burned Gas Zone Temperature |
| UHC | Unburned Hydrocarbons |
| Xgas | Fresh Mixture Composition |
| $Y_{res}$ | Residual Gas Mass Fraction |
| λ | Excess Air Ratio |
| CO | Carbon Monoxide |
| $CO_2$ | Carbon Dioxide |
| $H_2$ | Hydrogen |
| $H_2O$ | Water |
| HC | Hydrocarbons |
| $HCO^{\bullet}$ | Formyl Radical |
| $^{\bullet}HO_2$ | Hydroperoxyl Radical |
| $N_2$ | Nitrogen |
| $N_2O$ | Nitrous Oxide |
| $NH_3$ | Ammonia |
| NO | Nitric Oxide |
| $NO_2$ | Nitrogen Dioxide |
| $NO_X$ | Nitrogen Oxides |
| $O_2$ | Oxygen |
| $OH^{\bullet}$ | Hydroxyl Radical |
| THC | Total Unburned Hydrocarbons |
| $X_{CO}$ | CO Concentration |
| $X_{NO}$ | NO Concentration |

stabilizing combustion [14].

There are proposals for hydrogen-based vehicles (fuel cell and internal combustion engine vehicles) including hydrogen enrichment of conventional gasoline engines as an effective strategy to expand its utilization and adoption [15]. It has been reported that small additions of hydrogen can improve engine thermal efficiency and reduce carbon-based emissions [16,17]. By contrast, this strategy could increase nitrogen oxide ($NO_X$) formation [18]. A key impact of hydrogen enrichment is the significant increase in combustion speed mainly in the first stages of the combustion process [19]. This fast flame propagation promotes rapid and complete burning of the fuels, influencing the rate of energy release and, ultimately, affecting both engine performance and exhaust emissions characteristics. Furthermore, the broader flammability limits of hydrogen can enable Spark Ignition (SI) engine operation under lean conditions [11,20], by potentially enhancing combustion stability and efficiency while reducing carbon-based emissions. On a well-to-wheel basis, the overall impact will depend on the hydrogen source [21].

Cycle-to-cycle variations (CCV) are inherent inconsistencies in combustion parameters across consecutive engine cycles when the engine is working under the same operating conditions, resulting from mixture and flow inhomogeneities [22], and flame kernel variability [23]. CCV is higher in spark ignition engines than in compression ignition engines, since thermo-fluid dynamic processes are less stable in SI engines [24]. CCV directly affects engine performance and pollutant formation. Incomplete combustion in some cycles elevates unburned hydrocarbons (UHC) and CO [25], while higher temperatures in others increase nitrogen oxides ($NO_X$) [26,27]. Furthermore, CCV in exhaust gas composition and temperature can hinder catalytic converter efficiency, causing transient emission spikes [28]. Understanding and quantifying CCV is key for enhancing engine stability and efficiency, designing effective engine control strategies for minimizing overall emissions [29] and ensuring robust performance of aftertreatment systems across all engines operating conditions. This is particularly important for new fuels like hydrogen and complex gasoline-hydrogen fuel mixtures where combustion sensitivity to in-cylinder conditions can exacerbate CCV effects on emissions.

Previous investigations have examined the influence of CCV in NO emissions in compression ignition engines [30]. In such engines, the injection timing and duration impact the CCV in nitrogen oxide (NO) concentrations, reflecting differences with the CCV of the heat release rate (HRR) [30]. Reported NO concentration CCV values typically range from 15% to 25%, with only minor variations observed in HRR CCV under similar conditions [31]. Given that spark ignition engines are generally more susceptible to CCV in pressure signals than their compression ignition counterparts, it is reasonable to assume that this variability extends to exhaust emissions as well. Numerical appraisals of ammonia-hydrogen combustion in SI engines confirm this sensitivity, reporting NO concentration CoV values as high as 40%, despite peak temperature variations remaining near 1% [14]. Consequently, there is a clear need for further investigation into the influence of CCV on pollutant emissions in spark ignition engines. Existing literature also points to a scarcity of studies on the fundamental characteristics of hydrogen combustion processes within engine environments [32]. This research deficiency becomes even more pronounced when considering the complexities of gasoline and hydrogen mixtures [19] and the impact of hydrogen on emissions dispersion/variability.

This study aims to tackle those relevant scientific gaps, facilitating the following innovative aspects: i) Development of a novel chemical kinetic diagnostic framework enabling the understanding of the interplay between combustion variability and nitrogen-based emissions (e.g. NO, $N_2O$), CO and $H_2$; ii) Leveraging experimental in-cylinder pressure (spark ignition engine fuelled with various gasoline-hydrogen blends operating under a range of excess air ratios) to isolate the chemical kinetics of individual combustion cycles, beyond quasi-dimensional models predicting flame propagation; iii) Development of a custom chemical kinetic model fed by in-cylinder temperature profiles, crucially mapping out a new statistical relationship tying the residual gas fraction directly to NO cycle-to-cycle variability; iv) Providing a practical framework to deliver novel insights and quantification on how hydrogen fuel enrichment mitigates emissions instability, moving beyond traditional cycle-averaged studies. The significance of this digital framework is particularly strengthened for future powertrain operating under high efficiency conditions (i.e. lean in fuel), where emissions control remains

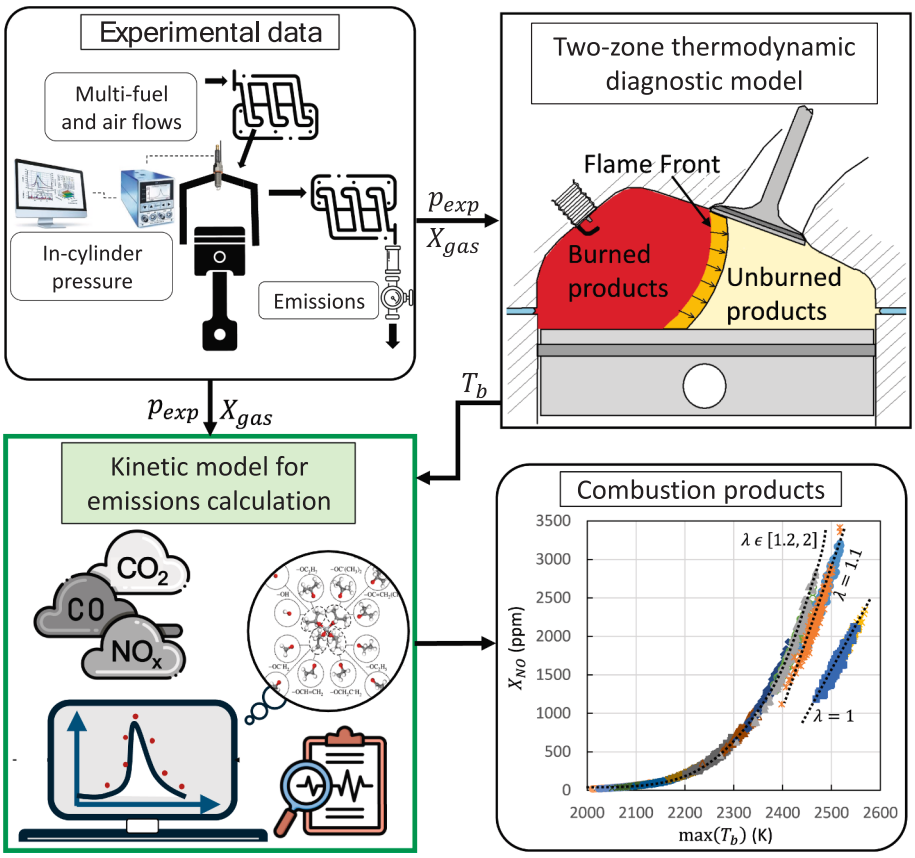


**Fig. 1.** Schematic of the chemical kinetic diagnostic methodology.

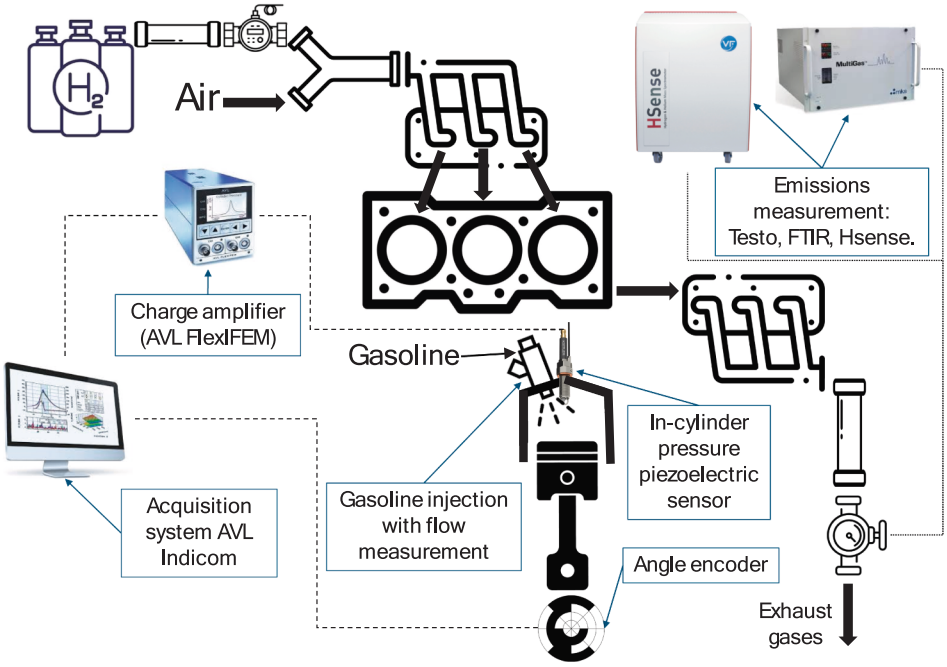


**Fig. 2.** Experimental facility schematic diagram.

a critical challenge.

## 2. Methodology

Fig. 1 presents a schematic of the methodology employed. The primary experimental inputs to the developed kinetic model are the instantaneous pressure ($P_{exp}$) and the feed flow rates, from which the fresh mixture composition ($X_{gas}$) is determined. Prior to its application in the kinetic model, the experimental data undergoes initial processing using a two-zone thermodynamic model. This two-zone thermodynamic

**Table 1**
Engine geometry specifications.

| Parameter | Value |
|---|---|
| Bore (D) x Stroke (S) | 84 x 90 mm |
| Number of Cylinders (Z) | 3 |
| Number of Valves | 12 |
| Displacement | 1497 $cm^3$ |
| Compression Ratio (CR) | 11:1 |
| Intake Valve Opening (IVO) | 20° |
| Intake Valve Closing (IVC) | −88° |
| Exhaust Valve Opening (EVO) | 92° |
| Exhaust Valve Closing (EVC) | 0° |
| Max Intake Valve Lift | 10 mm |
| Max Exhaust Valve Lift | 9 mm |

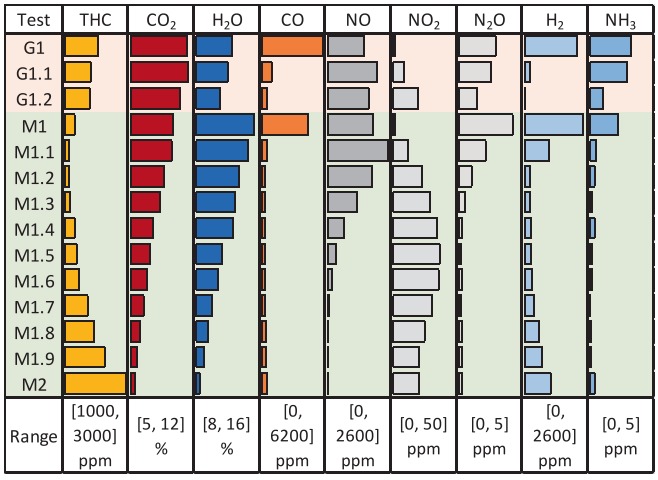


**Fig. 3.** Experimental measurement of pollutant emissions at each test point.

model subsequently yields the evolution rate of combustion products ($T_b$). Finally, the developed kinetic model enables the calculation of the burned product composition at each crank angle degree.

### 2.1. Experimental data

The experiments were carried out using a modern three-cylinder, four-stroke engine with spark ignition (SI) and gasoline direct injection (GDI). The engine intake system was specifically modified to allow for the injection of hydrogen as a fuel. An engine cylinder was instrumented with a high-resolution pressure transducer for in-cylinder pressure signal acquisition as a function of crank angle degree (CAD). The layout of the experimental facility is schematized in Fig. 2.

The main engine specifications can be found in Table 1 further information is detailed in [16].

The intake pressure was adjusted to achieve varying excess air ratios (λ), while maintaining a constant effective torque of 40 Nm and an engine speed of 2000 rpm. Spark timing was precisely controlled to ensure that 50% of the fuel mass was burned within the angular interval spanning from spark discharge to 5 CAD after top dead centre (ATDC) as in [19]. Two distinct fuel compositions were employed. The first set of experiments, designated 'G' (Gasoline), utilized commercial E10 gasoline (10% ethanol by volume), a standard fuel in the UK market. Concurrently, a second series of tests, labelled 'M' (Mixture), involved a hydrogen-gasoline blend. Both fuels are investigated at the same engine operation conditions as in [16].

Each individual test point is uniquely identified by its fuel designation (G or M) followed by its corresponding excess air ratio (λ). As an illustrative example, M1.1 represents the hydrogen-gasoline mixture tested at λ = 1.1. Hydrogen constituted approximately the 30% of the total energy input (10% hydrogen by mass) in 'M' blend, a proportion specifically chosen to ensure consistent engine speed and power output across all comparative experiments [19].

**Table 2**
Uncertainty percentages for measured emission data.

| Parameter/ Species | Instrument | Measurement Range | Uncertainty (%) |
|---|---|---|---|
| Cylinder Pressure | AVL Piezo-electric | 0–250 bar | ± 0.5% |
| Crank Angle | Baumer Encoder | 0–360 | ± 0.1 CAD |
| CO | MKS 2030 FTIR | 10 ppb – 100% FS | ± 3.0% |
| $NO_X$ | MKS 2030 FTIR | 0–5000 ppm | ± 3.0% |
| $N_2O$ | MKS 2030 FTIR | 0–200 ppm | ± 3.0% |
| $H_2$ | V&F H-Sense MS | 0.1–100 vol% | ± 2.0% |
| Brake Torque | Eddy Current Dyno | 0–240 Nm | ± 1.5% |

FS: Full Scale

Fig. 3 shows the experimental emission concentrations for each test conducted. Carbon monoxide (CO), carbon dioxide ($CO_2$), water ($H_2O$), nitrous oxide ($N_2O$), ammonia ($NH_3$), nitric oxide (NO), nitrogen dioxide ($NO_2$), and total hydrocarbons (THC) concentrations were measured using an MKS MultiGas 2030 Fourier Transform Infrared (FTIR) spectroscopy analyser. This technique leverages the principle of molecular infrared absorption to enable real-time concentration measurements of these gaseous species. Hydrogen ($H_2$) concentration measurements were performed via a V&F HSense analyser, which utilizes electron impact ionization mass spectrometry (EI-MS) for real-time monitoring of hydrogen levels. Data acquisition for gaseous species was conducted at a frequency of 1 Hz. It is observed (Fig. 3) that an increase in λ reduces the exhaust concentrations of both gases, primarily due to the higher presence of $O_2$ and $N_2$ in the exhaust stream. Furthermore, when comparing the G and M test at equivalent λ values, a decrease in $CO_2$ concentration is accompanied by an increase in $H_2O$ concentration when hydrogen is added to gasoline.

### 2.2. Uncertainty analysis and data reliability

To ensure the statistical significance of the diagnostic results and the observed emissions variability, an Nth-order uncertainty analysis was conducted following the Kline and McClintock method [33,34]. This approach allows for quantifying how individual sensor inaccuracies propagate into the final diagnostic parameters, such as the burned gas temperature ($T_b$). The cumulative uncertainty ($w_R$) for any parameter R derived from the independent measured variables ($x_1$, $x_2$, $x_3$, $x_n$) is calculated according to the Eq (1).

$$w_R = \sqrt{\left(\frac{\partial R}{\partial x_1} w_1\right)^2 + \left(\frac{\partial R}{\partial x_2} w_2\right)^2 + \cdots + \left(\frac{\partial R}{\partial x_n} w_n\right)^2} \quad (1)$$

The uncertainties for the primary instruments, based on the experimental facility characterization (Section 3), are detailed in Table 2.

The propagated uncertainty for IMEP and $T_b$ were estimated at ± 1.4% and ± 2.6%, respectively, using the method of sequential perturbations [34]. These precision levels confirm that the observed cycle-to-cycle variations are physically significant. Specifically, the measurement uncertainty for NO (±3.0%) is an order of magnitude lower than its recorded variability (up to 35%), validating that fluctuations represent in-cylinder kinetic phenomena rather than instrumental noise. Furthermore, the 5.11 m optical path length and high SNR (~450) of the FTIR system ensure reliable detection of low-concentration species such as $N_2O$ (below 5 ppm) in hydrogen-enriched lean combustion.

### 2.3. Two-zone thermodynamic diagnostic model

A two-zone thermodynamic model was employed to process the in-cylinder pressure data acquired during engine operation. This widely used approach [35,36] assumes the combustion chamber consists of two

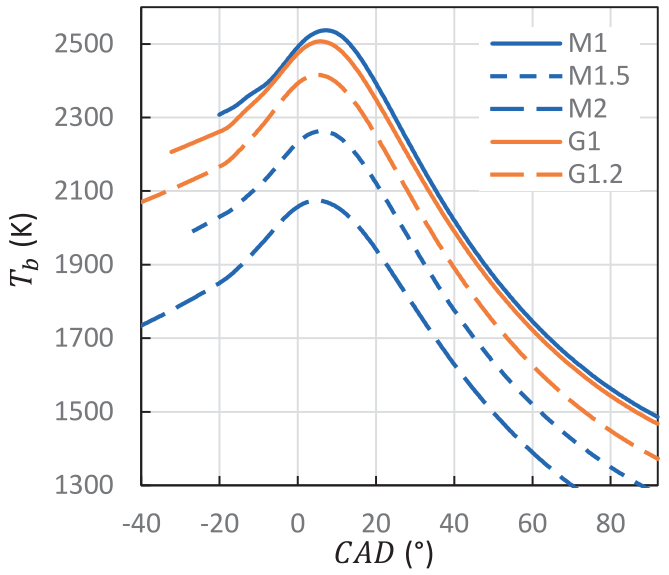


**Fig. 4.** Cycle-averaged $T_b$ evolution as a function of crank angle at different fuels and operating conditions.

physically distinct zones: one containing burned gases (combustion products) and the other the unburned fresh charge (reactants), separated by a thin flame front where chemical reactions occur. The model enables the determination of the heat release rate (HRR) and mass fraction burned (MFB) as functions of crank angle (CA), relying on experimental in-cylinder pressure measurements, the measured unburned gas input and the estimated residual gas. Prior to being introduced into the model, the pressure data are filtered [37] and corrected using a methodology based on genetic algorithms [38], which optimize the input parameters by minimizing the error associated with the diagnostic results. As the flame front propagates through the unburned mixture, it progressively transforms it into combustion products, increasing their internal energy due to the heat released during the reaction.

To estimate the thermodynamic properties within the burned gas zone, the model focuses on the species with larger concentrations: $CO_2$, $H_2O$, $N_2$, and $O_2$. It also considers the dissociation of $CO_2$ by including CO formation, assuming that all species are in chemical equilibrium [39]. This approach simplifies the calculations while still capturing the key chemical behaviour of the burned gases. The temperature evolution of the burned gas zone ($T_b$), obtained from the diagnostic model, is used in the kinetic model to estimate the composition of low concentration pollutant species. Although thermal stratification inherently occurs, at homogeneous burned gas zone is a well-established assumption in quasi-dimensional CCV diagnostics, as high turbulence mixing in SI engines justifies the use of a mean burned temperature to capture global emissions trends [26,40]. Furthermore, this framework provides the computational efficiency necessary to resolve the chemical kinetics of 200 consecutive cycles per operating point, which is essential for robust statistical analysis [41].

Fig. 4 shows the evolution of the burned gas zone temperature ($T_b$) as a function of crank angle degree. The values presented are cycle-averaged over 200 consecutive cycles for each operating point. As the excess air ratio (λ) increases, the amount of fuel introduced remains practically constant. However, due to the higher intake pressure [19], the energy released during combustion is similar across all operating points. This energy is distributed over a greater total mass, freed with a lower peak HRR and with a larger combustion duration as λ increases, resulting in lower $T_b$ values [19].

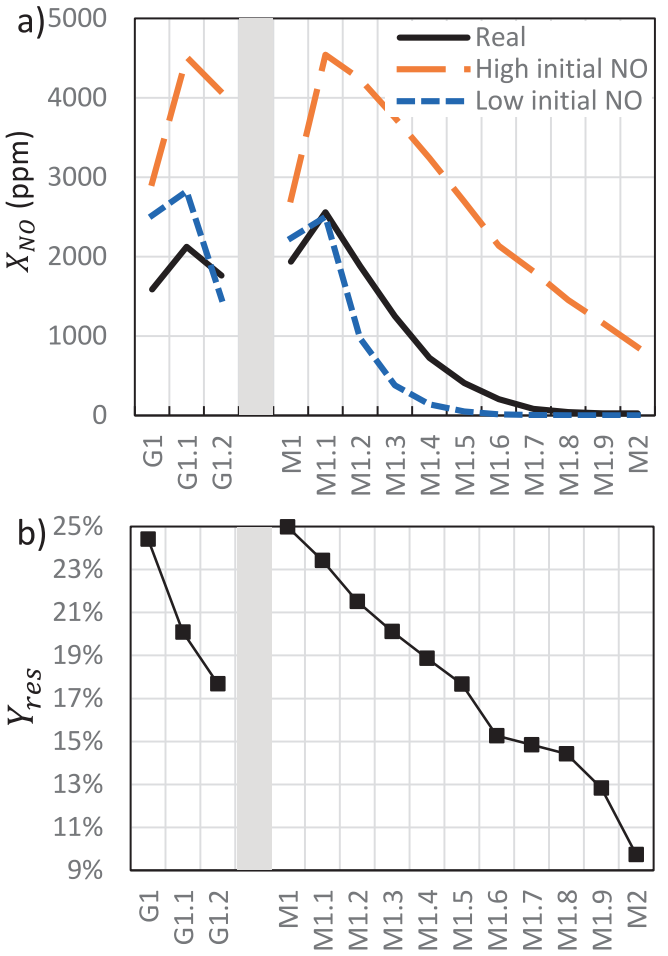


**Fig. 5.** NO prediction with the chemical kinetic model using different initial conditions. (b) Required residual mass fraction at each test point to match experimental NO emissions.

### 2.4. Chemical kinetic model

A chemical kinetic model has been developed to analyse the temporal evolution of combustion products within the burnt gas region. The proposed model posits that the concentration of each species at any given instant is independent of the mass traversing the flame front. This assumption is justified by the significantly larger magnitude of the existing mass within the burnt gas region after the spark ignition [19].

The chemical kinetic diagnostic model was implemented using the ideal gas reactor solver available in Cantera [42], through Python scripting, employing the chemical kinetic mechanism developed by Cai et al. [43]. This mechanism comprises 339 species and 2791 reactions and was calibrated explicitly for gasoline surrogate fuels. Optimized using rate rules, the mechanism integrates a reduced Primary Reference Fuel (PRF) sub-mechanism with a published kinetic model, enabling simulations of multi-component surrogates. It has been previously employed in the literature [20,44,45]. Isooctane was used as gasoline surrogate due to its well-characterized combustion properties and a laminar flame speed on the same order of magnitude as that of commercial gasoline [46].

Cycle-averaged data over 200 cycles were used for each experimental pressure and temperature point within the burnt gas region. The model requires an initial composition in the burnt gas region as a starting point for the calculations. Some authors set the initial composition of all non-major species ($CO_2$, $H_2O$, $N_2$, and $O_2$) to zero [47]. In this work, two approaches were followed: i) considering the initial composition to be that of equilibrium at spark discharge (High initial

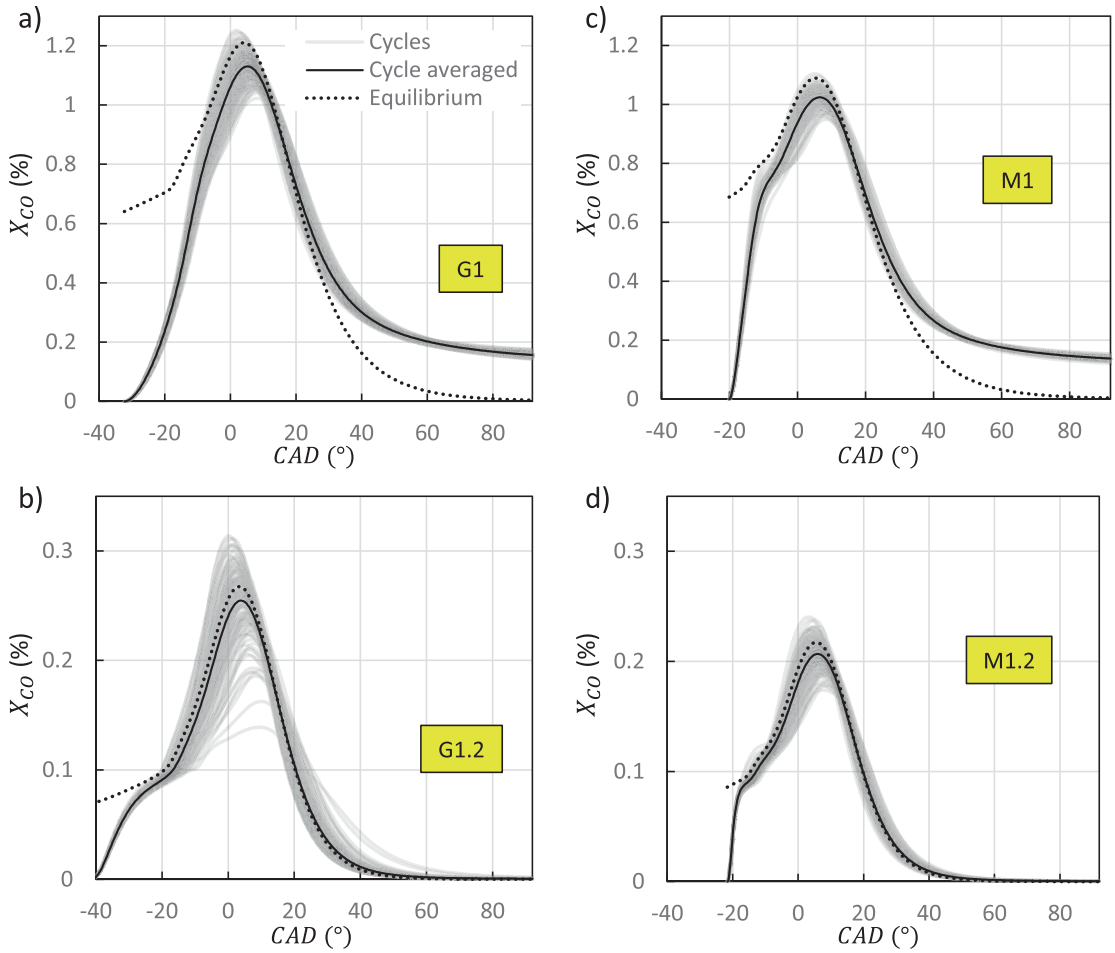


**Fig. 6.** Evolution of CO concentrations across all cycles for (a) G1; (b) G1.2; (c) M1 and (d) M1.2.

NO), ii) considering the composition to be that of equilibrium at ambient pressure and temperature (Low initial NO). Fig. 5 (a) shows the prediction results for the NO species using these two approaches as starting points, along with the experimental results obtained. It is observed that the Low initial NO option provides a better approximation of the experimental results and aligns more closely with the proposal of [47].

The results in Fig. 5 (a) were determined utilizing the residual mass fraction ($Y_{res}$), estimated simulating the gas exchange process through the AVL BOOST software. The same distribution layout used in the real engine was set, and the intake pressure was adjusted so that the resulting average mass flow rate matched the experimentally measured mass flow rate at each operating point, being consistent with previous studies [19]. Given the inherent challenges in accurately estimating the internal residual charge, $Y_{res}$ was utilized as a diagnostic calibration parameter. This approach leverages the high sensitivity of the NO formation mechanism to the in-cylinder thermal environment, providing a practical means to align predicted emissions with experimental measurements [48,49]. Modifying this fraction inherently alters the composition of the burned product, consequently impacting both the composition of the fresh mixture and the temperature of the burned gas. Specifically, an increase in the residual mass fraction leads to a decrease in the temperature of the burned product zone. Fig. 5 (b) presents the residual mass fraction ($Y_{res}$) for each test point, determined after adjusting the model to align the predicted NO concentration at the exhaust valve opening (EVO) with the experimental measurements. As λ increases, a corresponding decrease in $Y_{res}$ is observed. Conversely, the residual mass fraction exhibits an inverse relationship with intake pressure; it decreases as intake pressure rises aligning previous studies [50].

## 3. Results and discussion

The chemical kinetic diagnostic modelling framework is developed to analyse emissions variability (CO, $H_2$, NO and $N_2O$) as well as to understand the impact of hydrogen addition to gasoline fuel on emissions formation and their variability.

NO and $N_2O$ emissions formation mainly depend on chemical phenomena; thus, the composition of the fuel–air mixture was adjusted to ensure that the average NO and $N_2O$ emissions diagnosed with the model equal the experimental ones. However, CO and $H_2$ formation not only depend on chemical kinetics but are also influenced by physical phenomena of the fuel–air mixing and the combustion process. Thus, the developed framework enables a detailed study of CO and $H_2$ formation due to chemical kinetics and, by comparison with the experimental results, to study emissions formation due to physical phenomena.

### 3.1. Carbonaceous species and hydrogen

Fig. 6 shows the evolution of the modelled CO concentration per crank angle degree for each individual engine cycle, along with their average and the corresponding equilibrium values (dashed line). The instantaneous CO concentration (resolved per crank angle degree) generally follows the time-dependent equilibrium profile for each thermodynamic cycle. This indicates that both CO formation and oxidation reactions occur rapidly, with their reaction rates being the dominant factor governing its concentration, a behaviour known as being under kinetic control. This is particularly noticeable at lean combustion conditions ($\lambda > 1$), as the deviation of $X_{CO}$ from equilibrium

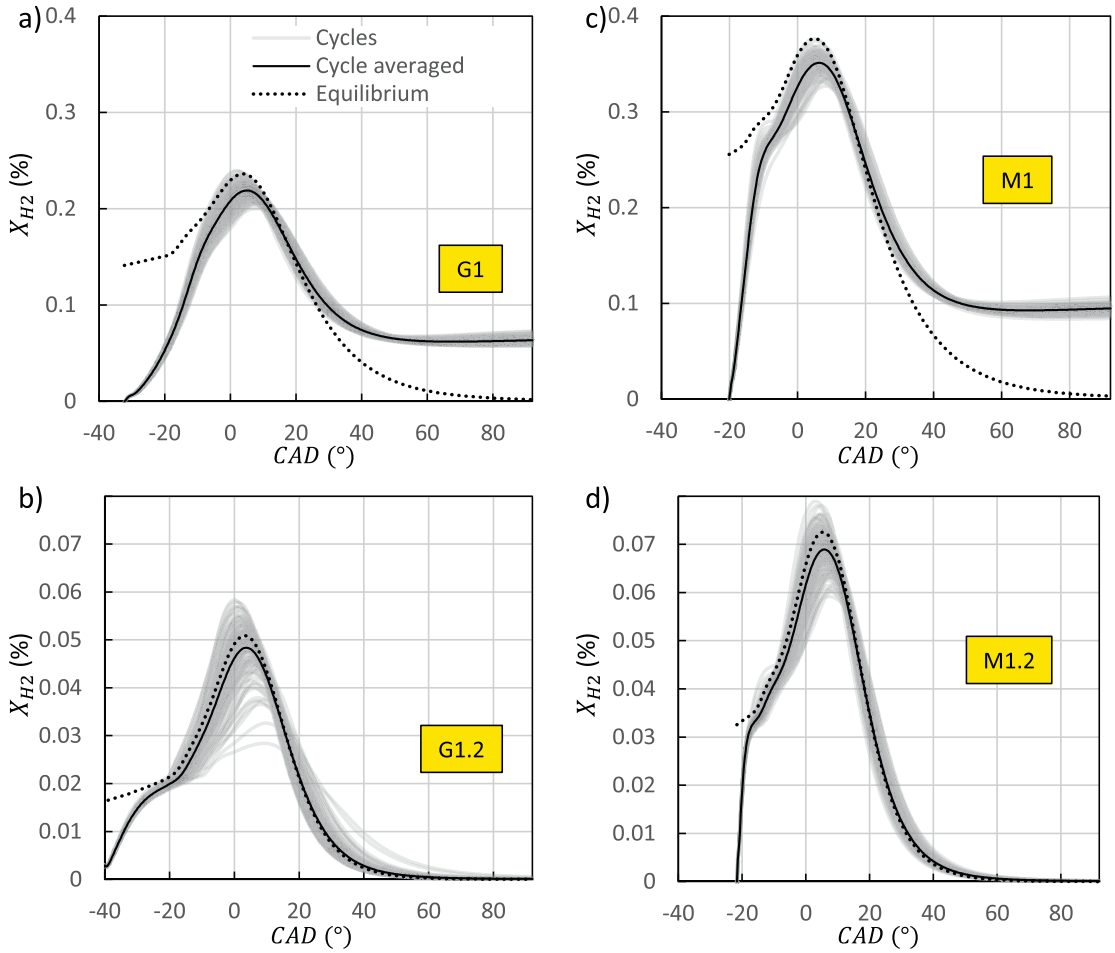


**Fig. 7.** Evolution of $H_2$ concentrations across all cycles for (a) G1; (b) G1.2; (c) M1 and (d) M1.2.

diminishes rapidly as the cycle progresses, suggesting a fast approach to equilibrium under oxygen-rich conditions. Furthermore, the predicted CO concentration at the end of the combustion process (EVO) is comparable to the equilibrium value, implying that under lean conditions, reaction rates remain sufficiently high to avoid significant departures from equilibrium (Fig. 6 (b) and (d)).

However, at stoichiometric condition ($\lambda = 1$), the predicted CO concentration at the end of the combustion process (EVO) exceeds its equilibrium value. It is thought that the reaction rates are slow, indicating a kinetic constraint ("freezing") and representing a potential source of CO emissions (Fig. 6 (a) and (c)). CO forms from the partial oxidation of the gasoline fuel components, generating intermediate radicals. Most of the proposed chemical kinetic mechanisms agree that the main pathway proceeds through the formyl radical ($HCO^{\bullet}$), which subsequently breaks down by reactions such $HCO^{\bullet} \leftrightarrow H + CO$ or $HCO^{\bullet} + O_2 \leftrightarrow CO + {}^{\bullet}HO_2$ [51–54]. Its final concentration is significantly influenced by subsequent oxidation to carbon dioxide through the reaction $CO + OH \leftrightarrow CO_2 + H$ [54]. Thus, the lack of $O_2$ at stoichiometric condition explains the freezing of kinetic reactions of CO destruction during the expansion stroke. When $\lambda > 1$ excess $O_2$ enhances $OH^{\bullet}$ radical formation, accelerating CO oxidation to $CO_2$, $CO + OH^{\bullet} \leftrightarrow CO_2 + H^{\bullet}$ [54].

CO cycle-to-cycle variability is observed along the cycle (crank angle degree). The final CO concentration exhibits remarkably low dispersion at the exhaust valve opening (CoV ≈ 4% at $\lambda = 1$). This low variability contrast with that of NO (discussed in Section 3.2), suggesting its formation is governed by more globally consistent phenomena rather than the extreme sensitivity to temperature fluctuations [26,55].

Fig. 7 shows the evolution of $H_2$ concentrations for the same conditions as Fig. 6. A similar kinetic trend to that of CO is observed. For lean conditions ($\lambda > 1$), $H_2$ concentration follows equilibrium values, indicating that chemical reactions do not "freeze" (Fig. 7 (b) and (d)). Conversely, a comparison of the stoichiometric ($\lambda = 1$) cases shows the hydrogen-enriched mixture (M1) results in higher final $H_2$ concentrations than the gasoline-only case (G1). This suggests that while the kinetic behaviour is analogous to CO, the final $H_2$ levels are also strongly influenced by fuel composition and physical phenomena, which require further analysis.

Consistent with the behaviour of CO, the final $H_2$ concentration shows minimal cycle-to-cycle variability (CoV approximately 5% when $\lambda = 1$). This low dispersion suggests that, like CO, its final concentration is dictated by more stable bulk phenomena rather than the highly transient conditions that affect other combustion products, such as NO.

A comprehensive understanding of CO and $H_2$ requires considering both chemical kinetics and distinct physical processes. These physical phenomena, contributing significantly to CO and $H_2$ EVO concentrations, include local air–fuel ratio (AFR) variations, fuel trapped in crevices (e.g., piston top-lands), flame quenching near combustion chamber walls, and fuel adsorption/desorption by oil films or deposits [56]. Such complex, three-dimensional physical mechanisms lead to incomplete combustion, which can be analysed by comparing the kinetic model results and the experimental results.

Fig. 8 compares the experimental and predicted concentrations of CO (Fig. 8 (a)), $H_2$, and unburnt hydrocarbon (THC) emissions (Fig. 8 (b)). The experimental measurements for CO, THC and $H_2$ are consistently higher than those calculated by the kinetic model. The model predicts

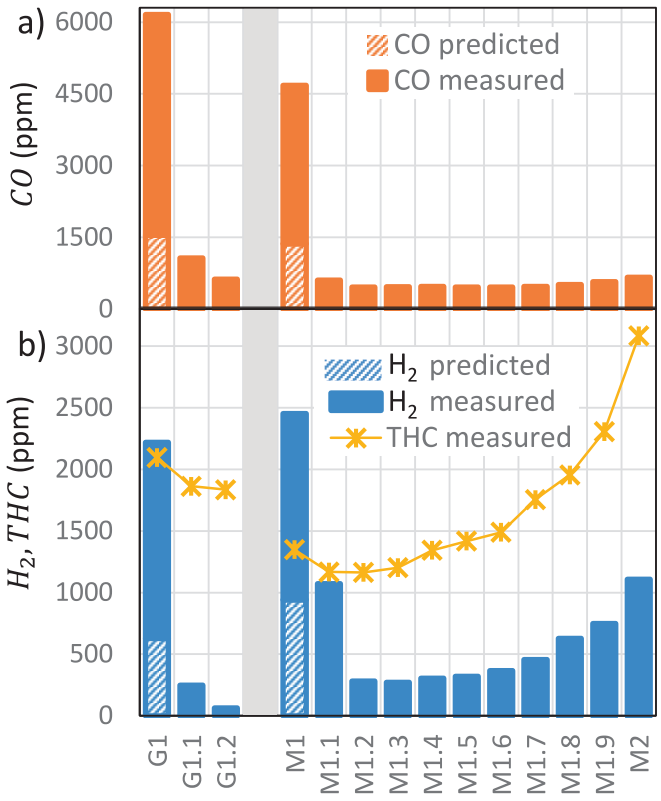


**Fig. 8.** Comparison of measured and chemical kinetic diagnostic model-predicted CO (a) and H2 (b) concentrations.

that all products in the burned gas zone have fully reacted, except when $\lambda = 1$ that CO, THC and $H_2$ concentrations increase due to the absence of O2. For the G1 test, $H_2$ EVO levels of approximately 2000 ppm were experimentally measured. During the gasoline combustion process, hydrogen is generated but not completely burnt, leading to its emission in the exhaust. For experimental measurements of hydrogen-gasoline mixtures (M), it is observed (Fig. 8) that as λ increases, CO and $H_2$ slightly rise. This effect can be attributed to flame quenching phenomena [57], resulting from lower burned product temperatures. This effect is also reflected, and more pronouncedly, in the measured THC emissions. The absolute discrepancies between diagnosed and measured are expected in two-zone diagnostic frameworks, as CO and $H_2$ levels are significantly governed by local phenomena, such as flame-wall quenching and crevice volumes [56,58], that fall outside the scope of bulk-gas kinetics.

### 3.2. Nitric oxide ($NO_X$) emissions

NO is primarily formed from the evolution of burned products at high pressure and temperature for a sufficient residence time [59]. The most significant pathway for NO and $NO_2$ formation is the thermal-$NO_X$ mechanism (also known as Zel'dovich mechanism), which involves the dissociation of $O_2$ at elevated temperatures (typically above 2000 K) and subsequent reactions of the resulting oxygen radicals with $N_2$ [60]. As shown in Fig. 3, NO emissions are approximately two orders of magnitude higher than $NO_2$ emissions. Consequently, due to the low concentration of $NO_2$ in exhaust gases, kinetic modelling of NO emissions typically yields more accurate results than modelling of $NO_2$ emissions.

### 3.3. NO formation during the cycle

Fig. 9 shows the calculated NO evolution from the chemical kinetic diagnostic model at each crank angle degree for all test points, the equilibrium concentration (dashed line) and the cycle-averaged value across all cycles. It is understood that NO emissions result from the "freezing" of the NO generation/destruction process [27]. Since each cycle evolves under different pressure and temperature conditions, the final NO emissions vary from cycle to cycle. This leads to observable cycle-to-cycle variations (CCV) in NO emissions.

To investigate the underlying causes of this variability, a Rate of Production (ROP) analysis was performed on the kinetics predicted by the diagnostic framework. Results are depicted in Fig. 10. A small group of five reactions among the forty involving NO accounts for approximately 85–95% of its formation and depletion kinetics, indicating a strong dominance of a limited number of pathways. Notably, the CCV in the net NO production rate (black line) appears to follow closely the CCV observed in individual reaction rates (grey lines), suggesting that fluctuations in specific kinetic steps are the primary drivers of the observed emissions variability. Furthermore, the ROP analysis reveals distinct kinetic trends depending on the λ value. At stoichiometric conditions ($\lambda = 1$, Fig. 10 (a) and (c)), the $N + O_2 \leftrightarrow NO + O$ reaction contributes marginally; however, its role becomes more pronounced under leaner conditions ($\lambda = 1.2$, Fig. 8b and 8d), likely due to the elevated $O_2$ levels that favour its progression. Finally, the analysis shows that beyond approximately 20°CA ATDC, reaction rates decline sharply, which is attributed to the post-combustion temperature drop leading to kinetic quenching or "freezing" of the relevant pathways.

### 3.4. NO emissions, cycle-to-cycle variability and phenomenology

Fig. 11 (a) shows the experimentally measured NO concentration as a function of the maximum burned product temperature predicted with the diagnostic model. The higher the temperature of the burned products, the greater the NO concentration, *especially under lean and stoichiometric conditions*. This aligns with what is described in the literature [15,61]. When operating at a stoichiometric excess air ratio ($\lambda = 1$), the scarcity of $O_2$ hinders NO generation. As a result, the NO concentration is lower in the G1 and M1 experiments compared to G1.1 and M1.1, despite having similar maximum temperatures of the burned product zone. Fig. 11 (a) further shows that NO emissions increase exponentially with the maximum burned gas temperature, indicating that fuels releasing a greater amount of energy in a shorter time (such as $H_2$) are susceptible to generating higher NO emissions if there is $O_2$ available.

Fig. 11 (b) depicts the exhaust NO concentrations as a function of the maximum burned product zone temperature for each experimental cycle. The observed trends are similar to those in Fig. 11 (a). Two phenomena converge in NO production: the burned product temperature and the λ value. At each test point, higher $T_b$ results in higher $X_{NO}$. Within this trend, for λ values in the range of [1.2, 2.0], the $X_{NO}$ values correlate with $T_b$, largely independent of the specific λ value within this range and the mixture composition. For $\lambda = 1.1$ (G1.1 and M1.1), $X_{NO}$ values at exhaust valve opening remain dependent on $T_b$. Compared to stoichiometric points ($\lambda = 1.0$), these $X_{NO}$ values are lower, primarily due to the slightly reduced maximum temperatures achieved at $\lambda = 1.1$, despite a higher overall oxygen availability. At $\lambda = 1$ (G1 and M1), the highest $X_{NO}$ concentrations are observed, consistent with peak combustion temperatures and the presence of oxygen radicals formed via dissociation at these extreme temperatures, both critical factors for the Zel'dovich mechanism.

Fig. 12 shows the coefficient of variation for NO emissions considering EVO concentration and the coefficient of variation of IMEP. When cross-referenced with Fig. 5 (a), it is observed that lower NO emissions correlate with a higher coefficient of variation. The coefficients of variation for NO emissions are found to range between 7% and 35%. These values are notably higher than the coefficients of variation for indicated mean effective pressure (IMEP) (typically less than 2%), which are conventionally employed to quantify cycle-to-cycle variations ($CCV_{IMEP}$). The CCV observed in pressure and temperature inherently leads to a more pronounced CCV in NO emissions.

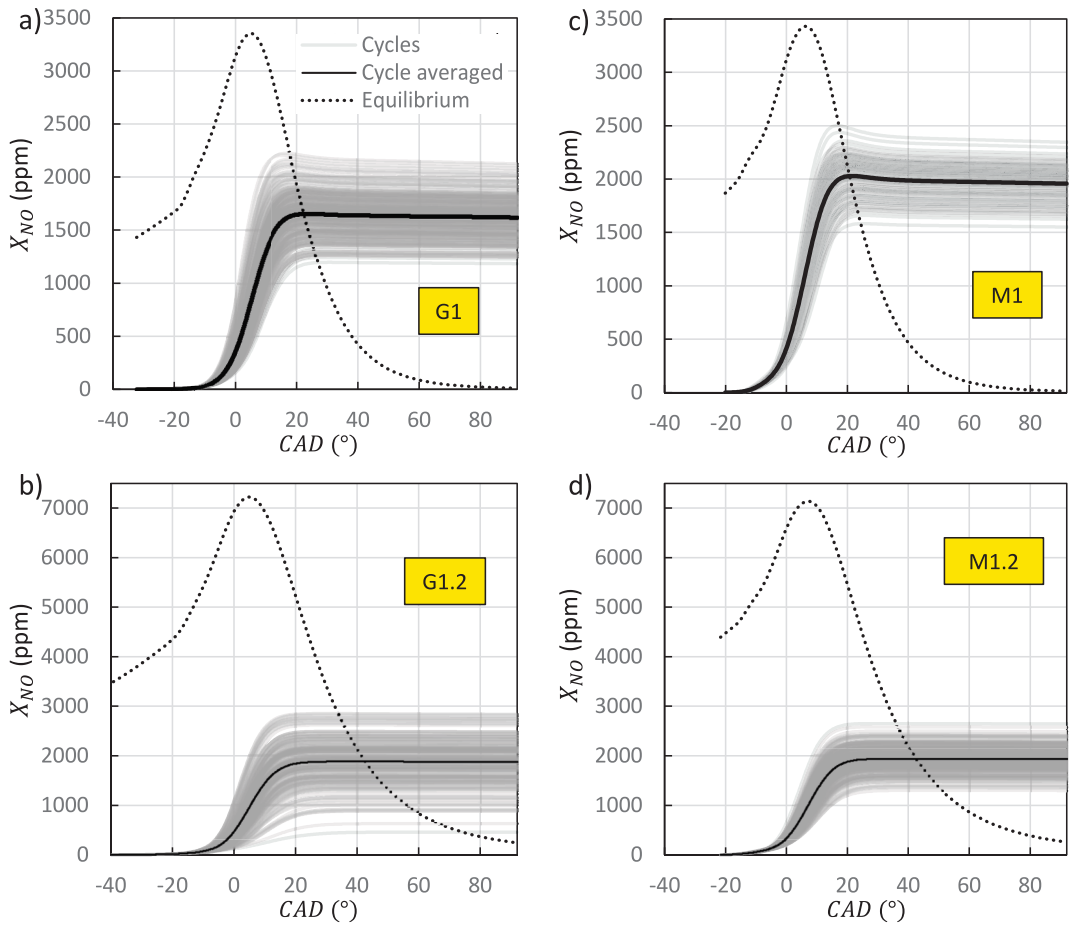


**Fig. 9.** Chemical kinetic diagnostic model-predicted NO concentration evolution at each crank angle degree for all test points. Equilibrium concentration (dashed line) and cycle-averaged values are also shown for (a) G1; (b) G1.2; (c) M1 and (d) M1.2.

The observed reduction in NO variability with hydrogen enrichment stems from an operational adaptation to the distinct thermochemical properties of the fuel leading into a more dilute engine operating state. This shift proves critical for achieving a homogeneous and stable combustion event. The entire causal chain is anchored by two core thermochemical traits of hydrogen: a potent Lower Heating Value (LHV) of ≈120 MJ/kg and its specific stoichiometric AFR of ≈34:1. Under constant torque conditions, an energy-equivalent substitution (accounting for gasoline with LHV≈42 MJ/kg and AFR≈14.7:1) required a reduced mass of hydrogen and air. This creates a twofold effect on the intake charge: the stoichiometric air demand drops (≈ 6%), and this reduction is compounded by the gaseous hydrogen physically displacing a portion of the intake air. As consequence the engine control system reduces the pressure in the intake manifold. This action impairs gas scavenging efficiency during the valve overlap period, leading to an inherently higher $Y_{res}$. This high internal dilution, which would typically destabilize gasoline combustion, creates a regime where the superior combustion characteristics of hydrogen provide a decisive advantage. Specifically, the high laminar flame speed of hydrogen and low ignition energy ensure a more rapid and robust initial flame kernel development [62], leading to a faster and more consistent overall combustion process [63,64]. This stabilizing effect is particularly pronounced under the dilute, low-load conditions established by operational adaptation of the engine [63]. So, the reduction in $CoV(X_{NO})$ is not just an emergent property of the dilute state, but a direct consequence of this synergetic interaction: the operational shift creates a challenging environment where the intrinsic ability of hydrogen to accelerate and stabilize combustion and hence NO formation.

### 3.5. Predicting NO emissions and cycle-to-cycle variability

Since CCV in NO emissions is higher than CCV in the other analysed emissions, a simplified predictive statistical model for NO emissions variability is proposed. For this, the distribution of the cycle-resolved data was investigated. As shown in Fig. 13, the NO concentrations at EVO demonstrate a distinct normal (Gaussian) distribution across the entire range of operating conditions analysed. This stochastic behaviour can be mathematically described by the Probability Density Function (PDF) and Cumulative Distribution Function (CDF) shown in Equation (1), where x corresponds to the NO emission value for each individual cycle.

$$PDF = \frac{1}{\sigma\sqrt{2\pi}} e^{-\frac{(x-\mu)^2}{2\sigma^2}}; CDF = \int PDF dx \tag{2}$$

Mean values, μ, and standard deviations, σ, are quantified in accordance with Eq. (2).

$$\mu = \frac{1}{N}\sum_{i=1}^{N} x_i; \sigma = \sqrt{\frac{\sum (x_i - \mu)^2}{N}} \tag{3}$$

The experimental data shows an excellent agreement with the fitted normal distributions, with relative errors consistently between 5% and 8% (Fig. 13). This high fidelity confirms that the entire stochastic profile of $CoV(X_{NO})$ emissions can be robustly described by just two statistical parameters: its mean (μ) and standard deviation (σ).

The predictive framework is constructed from two key statistical parameters. The first, the mean (μ), is obtained directly from cycle-

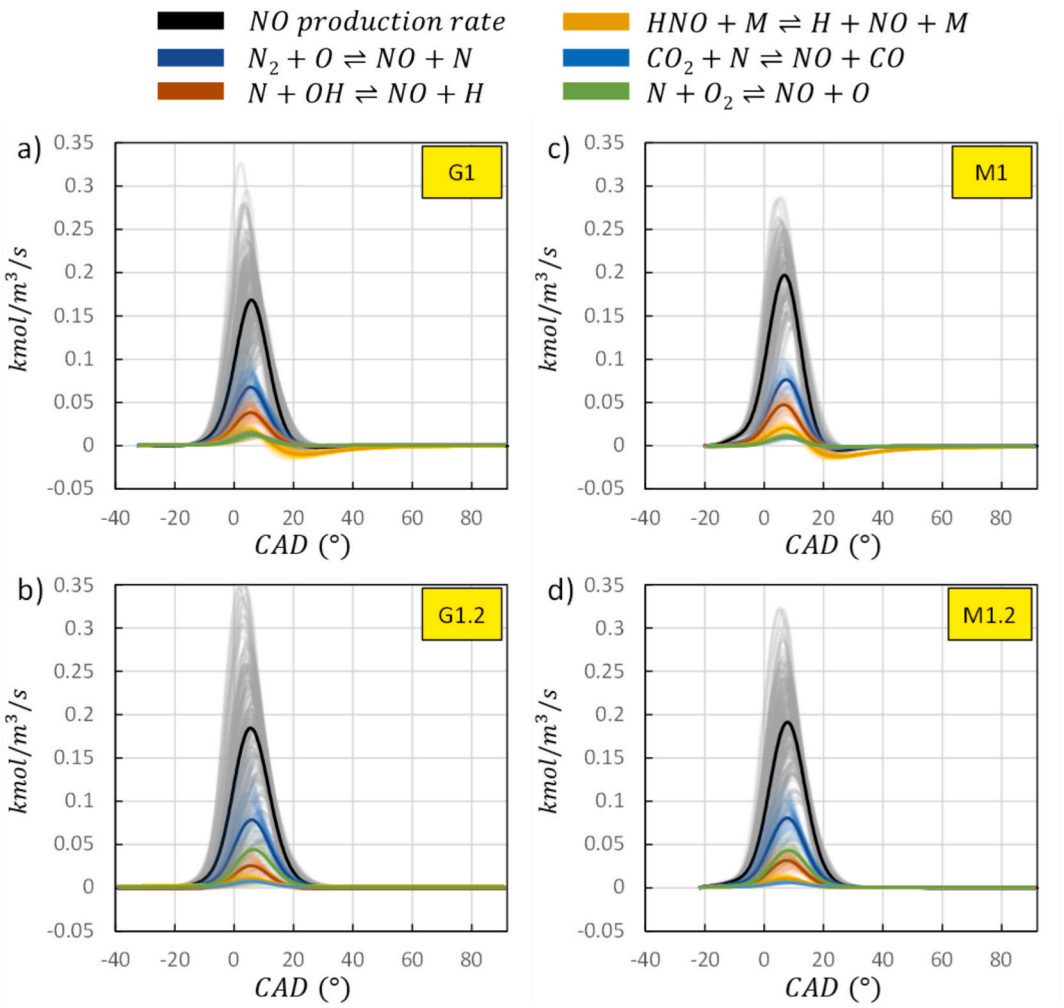


**Fig. 10.** ROP analysis of NO formation/destruction showing the five dominant reactions under different fuels (G, M) and equivalence ratios (λ = 1.0, 1.2) for all cycles. (a) G1; (b) G1.2; (c) M1 and (d) M1.2.

averaged experimental measurements, while the second, the standard deviation (σ), must be modelled to quantify the emissions dispersion. The determination of σ is achieved by first predicting the $CoV(X_{NO})$. Fig. 14 reveals a strong linear correlation between the $CoV(X_{NO})$ and the fresh mixture mass fraction (1- $Y_{res}$). Its coefficient of determination ($R^2$ = 0.94) justifies its application for predicting the $CoV(X_{NO})$ from the residual gas fraction. This allows the $CoV(X_{NO})$ to be reliably predicted from $Y_{res}$, which in turn allows for the calculation of the standard deviation according to Equation (3).

$$\sigma = \mu.CoV(X_{NO}); \sigma = \mu.(0.49 - 1.62Y_{res}) \quad (4)$$

To validate this framework, a predicted emissions envelope was defined. In accordance with the 68-95-99.7 empirical rule [65], the interval μ ± 3σ is expected to statistically contain 99.7% of all events for a normal distribution. This predicted envelope was then compared against the experimental data, as shown in Fig. 15. The predicted envelope (blue region) is shown to effectively capture the full range of dispersion observed between the experimental minimum and maximum NO values (dashed lines), which confirms the model's robustness in predicting the full range of NO emissions dispersion. Furthermore, the Fig. 15 visually demonstrates that while the NO dispersion envelope widens with increasing λ for gasoline (G tests), it systematically narrows for hydrogen-mixtures (M tests) at λ ≥ 1.1. This highlights a key finding: hydrogen addition reduces NO cycle-to-cycle variability under lean conditions.

Finally, although the empirical nature of the underlying correlation necessarily limits its direct application to the engine and specific conditions tested, the proposed framework constitutes a robust methodology. It successfully predicts the complete dispersion of NO emissions from a minimal set of input variables (averaged $X_{NO}$ and $Y_{res}$), making it a valuable tool for engine calibration and virtual design.

### 3.6. Nitrous oxide ($N_2O$) emissions

Fig. 16 depicts the relationship between average exhaust $N_2O$ concentration and the maximum temperature for each test point. The data indicate that $N_2O$ formation is negligible at low peak combustion product temperatures. A clear threshold emerges around 2400 K, beyond which $N_2O$ concentrations rise considerably, with higher temperatures leading to progressively elevated $N_2O$ levels.

The developed model successfully predicts the experimentally measured trends as a function of λ. However, the low $N_2O$ emission values hindered a comprehensive study of their CCV; therefore, the presented $N_2O$ results are cycle averaged. Fig. 17 presents the evolution of $N_2O$ concentration within the burned product zone, as calculated by the chemical kinetic diagnostic model, for test points G1, G1.2, M1, and M1.2 since for λ values higher than 1.2, $N_2O$ formation was found negligible. For comparison, equilibrium $N_2O$ concentrations are also shown (dotted line). Fig. 17 reveals that the evolution of $N_2O$ concentration in the burned product zone depends more significantly on λ than on the fuel composition.

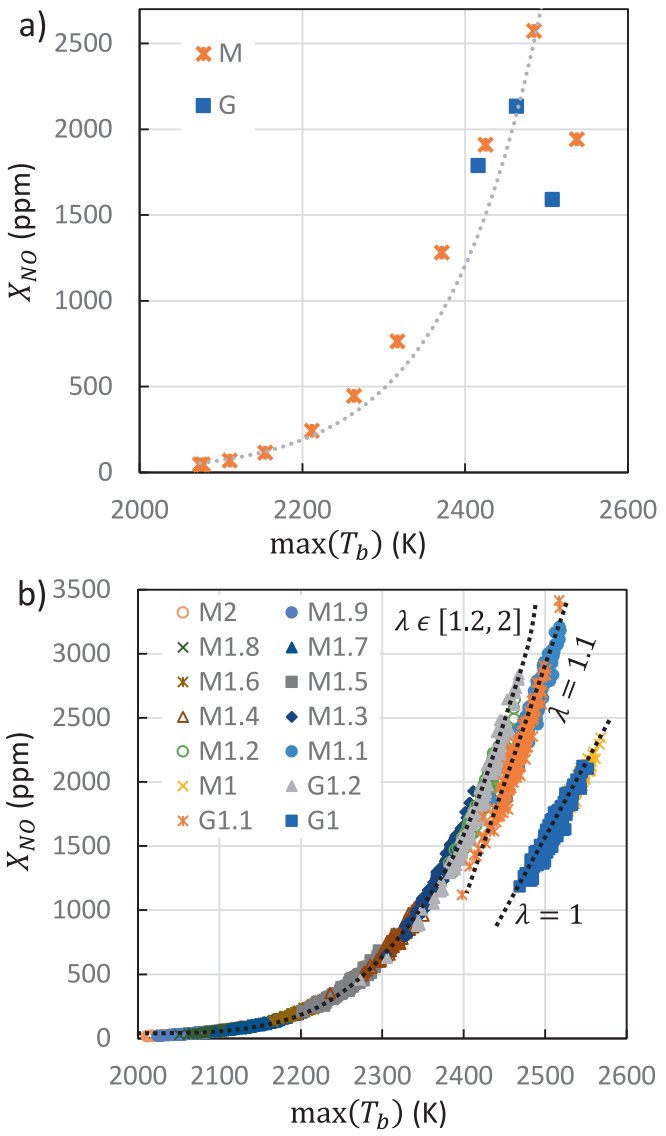


**Fig. 11.** (a) Exhaust NO concentration as a function of the maximum temperature of the burned zone for each test point for G (E10) and M (E10 + Hydrogen) fuel experiments. (b) Exhaust NO concentration as a function of the maximum burned product zone temperature for all cycles.

Further examination of Fig. 17 shows that from spark ignition until approximately 40 degrees ATDC, the $N_2O$ concentration predicted by the model closely matches the equilibrium concentration. During the main combustion event near TDC (approx. from −20 to 10 CAD), where in-cylinder temperatures peak, the model correctly captures a higher initial formation rate in lean conditions due to the greater availability of $N_2$ and $O_2$. However, during the subsequent expansion stroke (at later crank angles approx. From 10 to 40 CAD), where in-cylinder temperatures naturally decrease into a more moderate range, the kinetic balance shifts to strongly favour $N_2O$ destruction pathways [66]. In lean cases, the higher initial formation is followed by a more effective and prolonged destruction phase, facilitated by the lower post-combustion temperature profiles. This apparent contradiction is not a model deficiency but rather reveals the two-stage process governing net $N_2O$ emissions. Beyond 40 degrees ATDC, however, the predicted $N_2O$ concentration diverges significantly from the equilibrium value. This divergence indicates that the rapid drop in temperature leads to a thermal quenching of the destruction pathways (specifically the consumption by $H^{\bullet}$ radicals), a finding which aligns with the literature [67]. This implies that $N_2O$ levels are not actively formed at this stage but

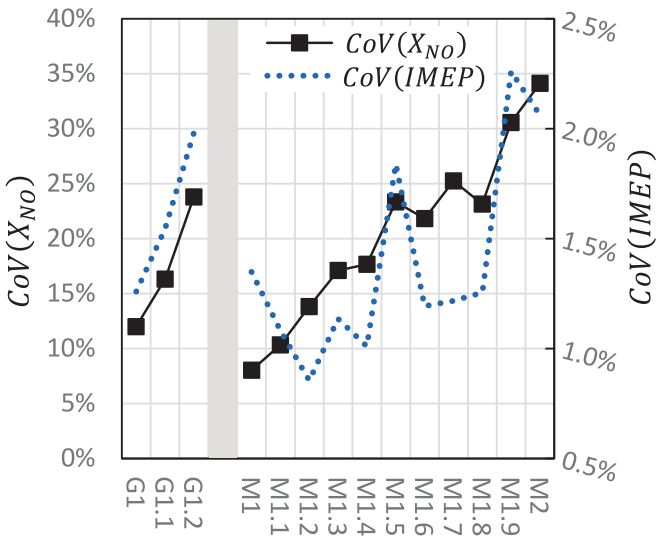


**Fig. 12.** NO concentration and IMEP coefficients of variation for each test point.

rather kinetically frozen at concentrations exceeding equilibrium values. Such kinetic freezing, occurring as in-cylinder temperatures decrease from their peak, is characteristic of the chemical destruction time scale exceeding the expansion time scale, becoming dominant over the high-temperature equilibrium pathways [68].

The final measured concentration at the exhaust (as shown in Fig. 3) is therefore the net result of this formation-destruction trade-off, suggesting that the critical parameter for $N_2O$ control is not the peak flame temperature, but the temperature–time history of the gases during the expansion stage.

## 4. Conclusions

This work has developed a novel chemical kinetic-diagnostic digital framework to quantify emissions' cycle-to-cycle variations (CCV), providing new insights into the impact of hydrogen-enriched combustion on emissions formation and their variability/dispersion. The application of this diagnostic framework yields the following key outcomes:

- The model accurately predicts CO, $H_2$, and nitrogen-based emissions, capturing the distinct roles of chemical kinetics and thermodynamic history.
- NO emissions exhibit strong variability (CoV of 7–35%), driven by the kinetic "freezing" of reactions tied to peak burned gas temperatures. Conversely, CO displays minimal CCV, and $N_2O$ formation is kinetically frozen during the expansion stroke rather than achieving chemical equilibrium.
- The dispersion of cycle-resolved NO concentrations follows a precise normal distribution. This statistical behaviour enables the robust prediction of NO variability based solely on the residual gas fraction ($Y_{res}$).
- Hydrogen enrichment significantly reduces NO CCV through a synergistic effect. Hydrogen enables an engine operational shift to higher internal dilution conditions (increased residual gases), where hydrogen's properties (e.g., high flame speed, low ignition energy) stabilise combustion without increasing overall NO formation.

Collectively, these insights and the proposed method provide a predictive framework to investigate solutions to reduce emissions variability, aiding the design of robust aftertreatment systems in future high-efficiency, lean-burn powertrains working with non-conventional fuels.

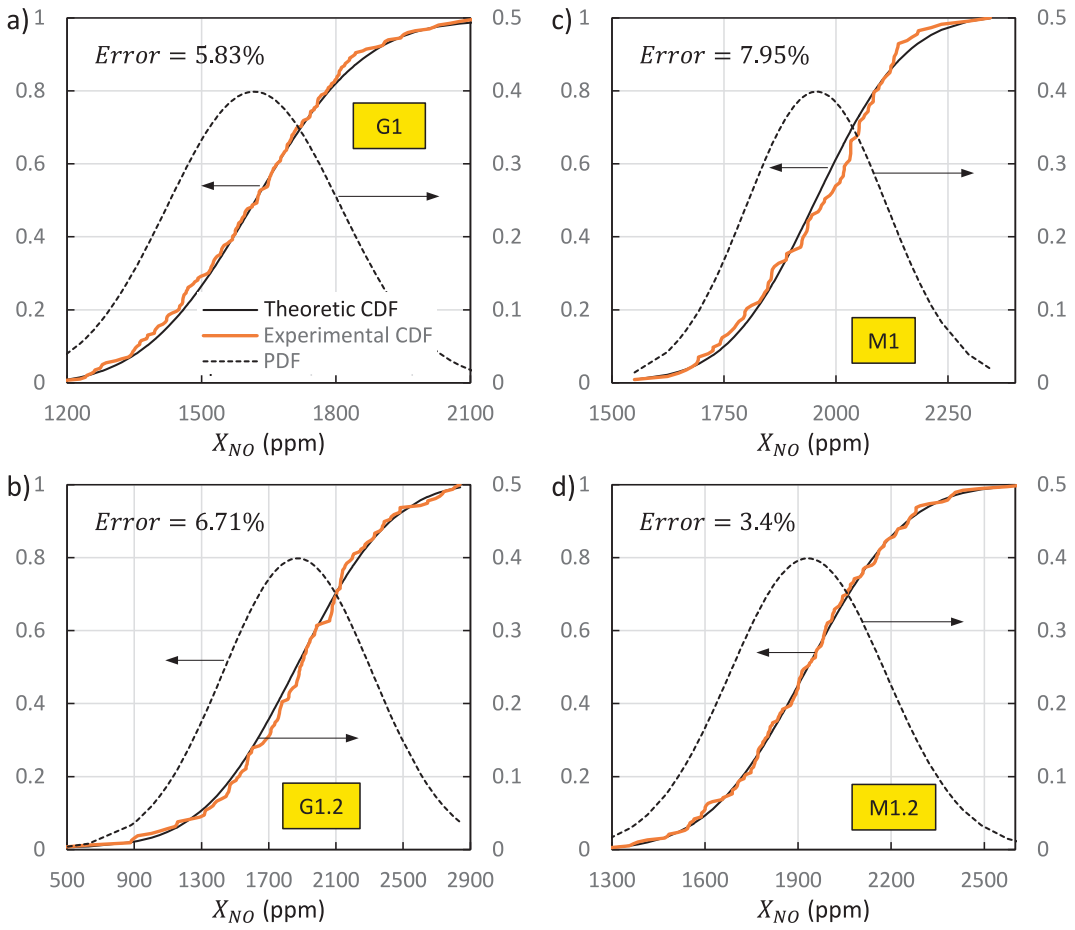


**Fig. 13.** Fitting of $X_{NO}$ values to normal distributions. (a) G1 test. (b) G1.2 test. (c) M1 test. (d) M1.2 tests.

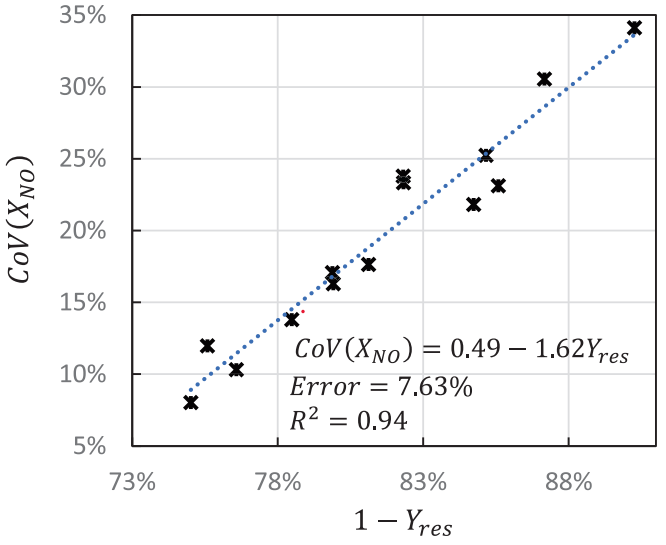


**Fig. 14.** Relationship between NO coefficient of variation ($CoV(X_{NO})$) and residual mass fraction ($Y_{res}$).

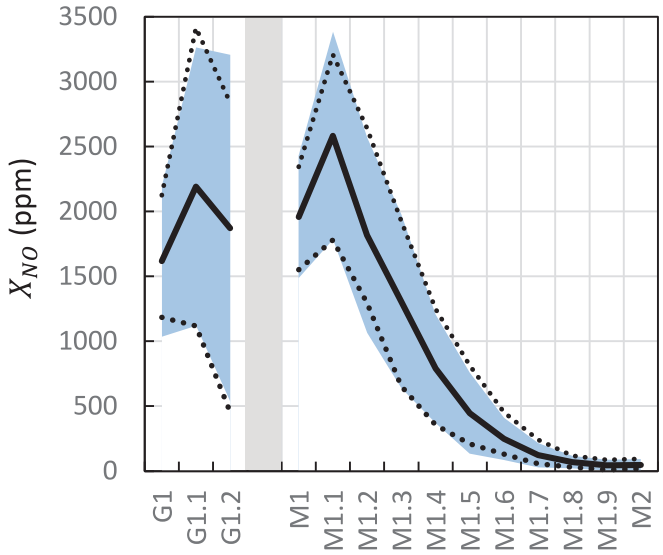


**Fig. 15.** Maximum and minimum NO concentrations for each test point considering a 99.7% confidence interval. Dashed lines are the maximum and minimum NO values, and the black continuous line is the experimental NO values measured.

## CRediT authorship contribution statement

**P. Gabana:** Writing – original draft, Software, Methodology, Formal analysis, Data curation, Conceptualization. **A. Cova-Bonillo:** Writing – original draft, Methodology, Formal analysis, Data curation, Conceptualization. **J.M. Herreros:** Writing – review & editing, Supervision, Project administration, Funding acquisition, Conceptualization. **A. Tsolakis:** Writing – review & editing, Supervision, Project administration, Funding acquisition, Conceptualization.

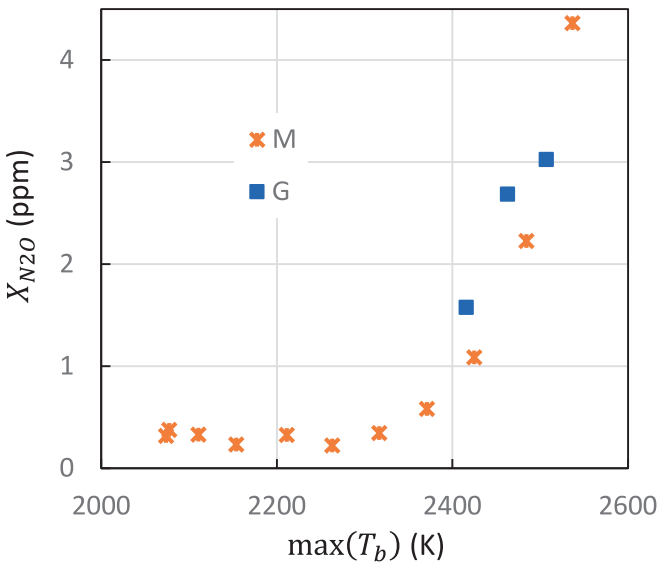


**Fig. 16.** Exhaust $N_2O$ concentration as a function of the maximum temperature of the burned zone temperature for G (E10) and M (E10 + Hydrogen) fuel experiments.

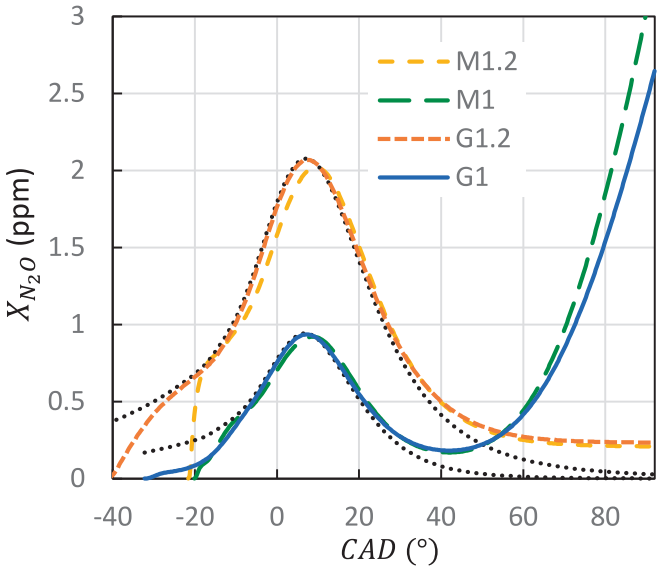


**Fig. 17.** Cycle-averaged $N_2O$ concentration evolution in the burned product zone for different test points. Equilibrium concentration values (dotted line) are also shown.

## Declaration of competing interest

The authors declare that they have no known competing financial interests or personal relationships that could have appeared to influence the work reported in this paper.

## Acknowledgements

ESPRC is acknowledged for supporting this work through the Mar-i$NH_3$ project (EPSRC Ref: EP/W016656/1). Thanks to the dedication of every researcher and technician in the Wyszynski Laboratory at the University of Birmingham.

Pedro Gabana Molina would like to thank the Spanish government funding through the project "Analysis and characterization of dual fuel combustion for the reduction of CO2 emissions in the transport sector" (PID2019-106957RB-C22). P. Gabana has been funded by the 2021 call for pre-doctoral contracts from the University of Valladolid, co-financed by Banco Santander.

The authors would like to thank AVL for providing access to its Advanced Simulation Technologies within the frame of University Partnership Program.

## Data availability

Data will be made available on request.

## References

[1] EEA, Greenhouse gas emissions from transport in Europe, (2024). https://www.eea.europa.eu/en/analysis/indicators/greenhouse-gas-emissions-from-transport?activeAccordion=546a7c35-9188-4d23-94ee-005d97c26f2b.
[2] Elegbeleye I, Oguntona O, Elegbeleye F. Green hydrogen: Pathway to net zero green house gas emission and global climate change mitigation. Hydrogen 2025;6:29. https://doi.org/10.3390/hydrogen6020029.
[3] Tasleem S, Alsharaeh EH. Role of green, yellow, blue, white and gold hydrogen in fuelling the path to net zero and sustainable future- A review. Energy Convers Manag 2025;326:119500. https://doi.org/10.1016/j.enconman.2025.119500.
[4] European Union, European Hydrogen Bank auction provides €720 million for renewable hydrogen production in Europe, (2024). https://ec.europa.eu/commission/presscorner/detail/en/ip_24_2333.
[5] Statista Research Department, Direct investment in hydrogen worldwide for 2030 as of October 2024, by project maturity, Statista (2025). https://www.statista.com/statistics/1478719/hydrogen-global-direct-investment-outlook/#statisticContainer.
[6] Onorati A, Payri R, Vaglieco BM, Agarwal AK, Bae C, Bruneaux G, et al. The role of hydrogen for future internal combustion engines. Int J Engine Res 2022;23:529–40. https://doi.org/10.1177/14680874221081947.
[7] Cecere G. Hydrogen as fuel for ICEs: State of art and technological challenges. J Eng 2024;2024:1–19. https://doi.org/10.1155/2024/9930258.
[8] Salvi BL, Subramanian KA. Sustainable development of road transportation sector using hydrogen energy system. Renew Sustain Energy Rev 2015;51:1132–55. https://doi.org/10.1016/j.rser.2015.07.030.
[9] Khalid AH, Muhamad Said MF, Veza I, Abas MA, Roslan MF, Abubakar S, et al. Hydrogen port fuel injection: Review of fuel injection control strategies to mitigate backfire in internal combustion engine fuelled with hydrogen. Int J Hydrogen Energy 2024;66:571–81. https://doi.org/10.1016/j.ijhydene.2024.04.087.
[10] Abubakar S, Muhamad Said MF, Abas MA, Ismail NA, Khalid AH, Roslan MF, et al. Hydrogen-fuelled internal combustion engines - Bibliometric analysis on research trends, hotspots, and challenges. Int J Hydrogen Energy 2024;61:623–38. https://doi.org/10.1016/j.ijhydene.2024.02.280.
[11] Novella R, Gomez-Soriano J, González-Domínguez D, Olaciregui O. Understanding the role of thermo-diffusive instabilities in hydrogen combustion for lean-burn spark-ignition engine operation. Energy Convers Manag 2025;334:119801. https://doi.org/10.1016/j.enconman.2025.119801.
[12] Purayil STP, Al-Omari SAB, Elnajjar E. Improving performance and hydrogen knock limit in SI engines using acetone–gasoline blends. Int J Hydrogen Energy 2026;199:152864. https://doi.org/10.1016/j.ijhydene.2025.152864.
[13] Purayil STP, Martini EA, Elsaid A, Khalil M, Zoghbour T, Seyam M, et al. Influence of steam induction on the performance and hydrogen knock limit of a hydrogen-gasoline spark ignition engine. Int J Thermofluids 2024;24:100933. https://doi.org/10.1016/j.ijft.2024.100933.
[14] Rakopoulos DC, Rakopoulos CD, Kosmadakis GM, Tutak W, Gruca M. Investigating the combustion, NO emissions and cyclic variability (CCV) in SI engine fueled with ammonia-hydrogen blends by two-zone quasi-dimensional model with two CCV governing mechanisms. Int J Hydrogen Energy 2025;184:151889. https://doi.org/10.1016/j.ijhydene.2025.151889.
[15] Purayil STP, Hamdan MO, Al-Omari SAB, Selim MYE, Elnajjar E. Review of hydrogen–gasoline SI dual fuel engines: Engine performance and emission. Energy Rep 2023;9:4547–73. https://doi.org/10.1016/j.egyr.2023.03.054.
[16] Yavuz M, Brinklow G, Cova Bonillo A, Herreros JM, Wu D, Doustdar O, et al. Alcove clave, the suitability of the three-way catalyst for hydrogen fuelled engines. Johnson Matthey Technol Rev 2024;68:412–26. https://doi.org/10.1595/205651324x17054113843942.
[17] Teoh YH, How HG, Le TD, Nguyen HT, Loo DL, Rashid T, et al. A review on production and implementation of hydrogen as a green fuel in internal combustion engines. Fuel 2023;333:126525. https://doi.org/10.1016/j.fuel.2022.126525.
[18] P. Singh, S. Sahoo, N.K.P. Singh, Hydrogen-Fueled Spark Ignition Engines: Understanding NOx Formation and Mitigation Through Engine Design Innovations, in: Ammonia and Hydrogen for Green Energy Transition, Springer, Singapore, 2024: pp. 371–392. https://doi.org/10.1007/978-981-97-0507-8_15.
[19] Gabana P, Giménez B, Martín Herreros J, Tsolakis A. Analysis of the combustion speed in a spark ignition engine fuelled with hydrogen and gasoline blends at different air fuel ratios. Fuel 381 2025. https://doi.org/10.1016/j.fuel.2024.133563.
[20] Liu Z, He X, Zhao C, Zhou X. Experimental and kinetic of hydrogen blending effects on lean flammability limit of gasoline fuels. Fuel 2025;384. https://doi.org/10.1016/j.fuel.2024.133936.

[21] Incer-Valverde J, Korayem A, Tsatsaronis G, Morosuk T. "Colors" of hydrogen: Definitions and carbon intensity. Energy Convers Manag 2023;291. https://doi.org/10.1016/j.enconman.2023.117294.
[22] Zhuang H, Hung DLS. Characterization of the effect of intake air swirl motion on time-resolved in-cylinder flow field using quadruple proper orthogonal decomposition. Energy Convers Manag 2016;108:366–76. https://doi.org/10.1016/j.enconman.2015.10.080.
[23] Duan X, Feng L, Xia Y. The mechanism and effect factors of the combustion cycle-to-cycle variations in the spark ignition engine. Energy Sci Eng 2024:4773–87. https://doi.org/10.1002/ese3.1879.
[24] Payri F, Luján JM, Martín J, Abbad A. Digital signal processing of in-cylinder pressure for combustion diagnosis of internal combustion engines. Mech Syst Sig Process 2010;24:1767–84. https://doi.org/10.1016/j.ymssp.2009.12.011.
[25] Watson HC, Goldsworthy LC, Milkins EE. Cycle by cycle variations of HC, CO, and NOX. SAE Technical Papers 1976. https://doi.org/10.4271/760753.
[26] Rakopoulos CD, Rakopoulos DC, Kosmadakis GM, Zannis TC, Kyritsis DC. Studying the cyclic variability (CCV) of performance and NO and CO emissions in a methane-run high-speed SI engine via quasi-dimensional turbulent combustion modeling and two CCV influencing mechanisms. Energy 2023;272:127042. https://doi.org/10.1016/j.energy.2023.127042.
[27] Karvountzis-Kontakiotis AT, Ntziachristos L. A detailed chemical mechanism to predict NO Cycle-to-cycle Variation in homogeneous engine combustion. IFAC 2012. https://doi.org/10.3182/20121023-3-FR-4025.00046.
[28] Bohm M, Stetina J, Svida D. Exhaust gas temperature pulsations of a gasoline engine and its stabilization using thermal energy storage system to reduce emissions. Energies (Basel) 2022;15. https://doi.org/10.3390/en15072365.
[29] Kosmadakis GM, Rakopoulos DC, Rakopoulos CD. Assessing the cyclic-variability of spark-ignition engine running on methane-hydrogen blends with high hydrogen contents of up to 50%. Int J Hydrogen Energy 2021;46:17955–68. https://doi.org/10.1016/j.ijhydene.2021.02.158.
[30] Kyrtatos P, Zivolic A, Brückner C, Boulouchos K. Cycle-to-cycle variations of NO emissions in diesel engines under long ignition delay conditions. Combust Flame 2017;178:82–96. https://doi.org/10.1016/j.combustflame.2016.12.025.
[31] Ioannou M, Papalambrou G, Kyrtatos NP, Larsson D, Matlok S, Mayer S. Crank-angle resolved NOx measurements from a specific engine cylinder of a large marine two-stroke engine. J Marine Eng Technol 2014;13:12–20. https://doi.org/10.1080/20464177.2014.11020295.
[32] Verhelst S, Wallner T. Hydrogen-fueled internal combustion engines. Prog Energy Combust Sci 2009;35:490–527. https://doi.org/10.1016/j.pecs.2009.08.001.
[33] O.R. Mohsen, MahmoudA. Mashkour, M.S. Gad, Energy-exergy analysis of butanone-gasoline blends with hybrid nanoparticles in a spark ignition engine, Case Studies in Thermal Engineering 73 (2025) 106597. https://doi.org/10.1016/j.csite.2025.106597.
[34] Moffat RJ. Describing the uncertainties in experimental results. Exp Therm Fluid Sci 1988;1:3–17. https://doi.org/10.1016/0894-1777(88)90043-X.
[35] Li RC, Zhu GG, Men Y. A two-zone reaction-based combustion model for a spark-ignition engine. Int J Engine Res 2021;22:109–24. https://doi.org/10.1177/1468087419841746.
[36] Wang Y. A novel two-zone thermodynamic model for spark-ignition engines based on an idealized thermodynamic process. Energies (Basel) 2020;13. https://doi.org/10.3390/en13153801.
[37] Gabana P, Giménez B, Melgar A, Horrillo A. Adaptive polynomial filter applied to in-cylinder pressure signal in internal combustion engines. Mech Syst Sig Process 2025;235:112871. https://doi.org/10.1016/j.ymssp.2025.112871.
[38] Reyes M, Melgar A, Pérez A, Giménez B. Study of the cycle-to-cycle variations of an internal combustion engine fuelled with natural gas/hydrogen blends from the diagnosis of combustion pressure. Int J Hydrogen Energy 2013;38:15477–87. https://doi.org/10.1016/j.ijhydene.2013.09.071.
[39] Giménez B, Melgar A, Horrillo A, Tinaut FV. A correlation for turbulent combustion speed accounting for instabilities and expansion speed in a hydrogen-natural gas spark ignition engine. Combust Flame 2021;223:15–27. https://doi.org/10.1016/j.combustflame.2020.09.026.
[40] Agarwal A, Filipi ZS, Assanis DN, Baker DM. Assessment of single- and two-zone turbulence formulations for quasi-dimensional modeling of spark-ignition engine combustion. Combust Sci Technol 1998;136:13–39. https://doi.org/10.1080/00102209808924163.
[41] Netzer C, Pasternak M, Seidel L, Ravet F, Mauss F. Computationally efficient prediction of cycle-to-cycle variations in spark-ignition engines. Int J Engine Res 2020;21:649–63. https://doi.org/10.1177/1468087419856493.
[42] Goodwin D, Speth R, Moffat H, Weber B. Cantera: An object-oriented software toolkit for chemical kinetics, thermodynamics, and transport processes. Zenodo 2021. https://doi.org/10.5281/zenodo.4527812.
[43] Cai L, Pitsch H. Optimized chemical mechanism for combustion of gasoline surrogate fuels. Combust Flame 2015;162:1623–37. https://doi.org/10.1016/j.combustflame.2014.11.018.
[44] Hann S, Grill M, Bargende M. Reaction kinetics calculations and modeling of the laminar flame speeds of gasoline fuels. SAE Technical Papers 2018-April (2018): 1–18. https://doi.org/10.4271/2018-01-0857.
[45] Wang X, Zhou F, Fu J, Liu J. Effect of ethanol on auto-ignition characteristics and laminar burning velocity of gasoline under elevated temperature and pressure. Fuel Process Technol 2023;242:107644. https://doi.org/10.1016/j.fuproc.2022.107644.
[46] Chu H, Xiang L, Nie X, Ya Y, Gu M, Jiaqiang E. Laminar burning velocity and pollutant emissions of the gasoline components and its surrogate fuels: A review. Fuel 2020;269:117451. https://doi.org/10.1016/j.fuel.2020.117451.
[47] Horrillo A. Utilizacion de modelos multizona para la prediccion de las emisiones contaminantes de escape en motores de encendido provocado, PhD Thesis. University of Valladolid; 1998.
[48] Lipardi ACA, Bergthorson JM, Bourque G. NOx emissions modeling and uncertainty from exhaust-gas-diluted flames. J Eng Gas Turbine Power 2016;138. https://doi.org/10.1115/1.4031603.
[49] Zareei J, Rohani A, Nuñez Alvarez JR. The effect of EGR and hydrogen addition to natural gas on performance and exhaust emissions in a diesel engine by AVL fire multi-domain simulation, GPR model, and multi-objective genetic algorithm. Int J Hydrogen Energy 2022;47:21565–81. https://doi.org/10.1016/j.ijhydene.2022.04.294.
[50] Fox JW, Cheng WK, Heywood JB. A model for predicting residual gas fraction in spark-ignition engines. SAE Technical Paper 1993. https://doi.org/10.4271/931025.
[51] Yang C, Zheng Z. Construction of a chemical kinetic model of five-component gasoline surrogates under lean conditions. Molecules 2022;27. https://doi.org/10.3390/molecules27031080.
[52] Zhen X, Wang Y, Liu D. An overview of the chemical reaction mechanisms for gasoline surrogate fuels. Appl Therm Eng 2017;124:1257–68. https://doi.org/10.1016/j.applthermaleng.2017.06.101.
[53] Yang S, Wang Q, Curran HJ, Jia M. Development of a 5-component gasoline surrogate model using recent advancements in the detailed H2/O2/CO/C1-C3 mechanism for decoupling methodology. Fuel 2021;283:118793. https://doi.org/10.1016/j.fuel.2020.118793.
[54] Curran HJ. Developing detailed chemical kinetic mechanisms for fuel combustion. In: Proceedings of the Combustion Institute 37; 2019. p. 57–81. https://doi.org/10.1016/j.proci.2018.06.054.
[55] Kosmadakis GM, Rakopoulos DC, Rakopoulos CD. Performance and emissions of a methane-fueled spark-ignition engine under consideration of its cyclic variability by using a computational fluid dynamics code. Fuel 2019;258:116154. https://doi.org/10.1016/j.fuel.2019.116154.
[56] Malfi E, Esposito S, De Felice M, Pitsch H, Pischinger S, De Bellis V. Phenomenological model for unburned hydrocarbon emissions from spark-ignition, pre-chamber, and dual-fuel internal combustion engines. Int J Engine Res 2024;25:1818–34. https://doi.org/10.1177/14680874241255157.
[57] Suckart D, Linse D, Schutting E, Eichlseder H. Experimental and simulative investigation of flame–wall interactions and quenching in spark-ignition engines. Automot Engine Technol 2017;2:25–38. https://doi.org/10.1007/s41104-016-0015-z.
[58] Esposito S, Diekhoff L, Pischinger S. Prediction of gaseous pollutant emissions from a spark-ignition direct-injection engine with gas-exchange simulation. Int J Engine Res 2021;22:3533–47. https://doi.org/10.1177/14680874211005053.
[59] Baratta M, Ferrari A, Zhang Q. Multi-zone thermodynamic modeling of combustion and emission formation in CNG engines using detailed chemical kinetics. Fuel 2018;231:396–403. https://doi.org/10.1016/j.fuel.2018.05.088.
[60] Lavole GA, Heywood JB, Keck JC. Experimental and theoretical study of nitric oxide formation in internal combustion engines. Combust Sci Technol 1970;1:313–26. https://doi.org/10.1080/00102206908952211.
[61] Al-Harbi AA, Alabduly AJ, Alkhedhair AM, Alqahtani NB, Albishi MS. Effect of operation under lean conditions on NOx emissions and fuel consumption fueling an SI engine with hydrous ethanol–gasoline blends enhanced with synthesis gas. Energy 2022;238. https://doi.org/10.1016/j.energy.2021.121694.
[62] Sun X, Liu H, Duan X, Guo H, Li Y, Qiao J, et al. Effect of hydrogen enrichment on the flame propagation, emissions formation and energy balance of the natural gas spark ignition engine. Fuel 2022;307:121843. https://doi.org/10.1016/j.fuel.2021.121843.
[63] Zhang B, Wang S, Zhai Y. Estimating the charge burning velocity within a hydrogen-enriched gasoline engine. Int J Hydrogen Energy 2023;48:10264–71. https://doi.org/10.1016/j.ijhydene.2022.12.154.
[64] Shivaprasad K, Chitragar P, Kumar G. Effect of Hydrogen addition on combustion and emission characteristics of high speed spark ignition engine- an experimental study, in. SAE Technical Paper 2015:141–8. https://doi.org/10.4271/2015-01-1684.
[65] Tijms H. Understanding probability. 3rd Edition. Cambridge University Press; 2012.
[66] Northrop WF. Modeling nitrogen species from ammonia reciprocating engine combustion in temperature-equivalence ratio space. Appl Energy Combust Sci 2024;17:100245. https://doi.org/10.1016/j.jaecs.2023.100245.
[67] Xie M, Li Q, Fu J, Yang H, Wang X, Liu J. Chemical kinetic investigation on NOx emission of SI engine fueled with gasoline-ethanol fuel blends. Sci Total Environ 2022;831:154870. https://doi.org/10.1016/j.scitotenv.2022.154870.
[68] Zhuang Z, Guan B, Chen J, Zheng C, Zhou J, Su T, et al. Review of nitrous oxide direct catalytic decomposition and selective catalytic reduction catalysts. Chem Eng J 2024;486. https://doi.org/10.1016/j.cej.2024.150374.